Research Article

Nano Research
2022, 15(9): 8648–8655

ISSN 1998-0124 CN 11-5974/O4
https://doi.org/10.1007/s12274-022-4456-6

Large-scale preparation of high-performance boron nitride/aramid nanofiber dielectric composites

Liying Su[1], Xiaoyan Ma[2], Jiale Zhou[1], Xiangchen Liu[3], Fanglin Du[1], and Chao Teng[1] (✉)

[1] *College of Materials Science and Engineering, Qingdao University of Science and Technology, Qingdao 266042, China*
[2] *College of Chemical Engineering, Qingdao University of Science and Technology, Qingdao 266042, China*
[3] *Weihai Jin Hong Group Co., Ltd., Weihai 264211, China*

Received: 12 March 2022 / **Revised:** 3 April 2022 / **Accepted:** 20 April 2022

ABSTRACT

Dielectric polymers featuring high thermal conductivity, excellent mechanical, and stable dielectric properties over a broad temperature range have attracted extensive scientific attention. In this work, a large-scale, layered film was fabricated using blade-coating approach, which integrated aramid nanofibers (ANFs) and boron nitride nanosheets (BNNSs) through a typical sol-gel transformation procedure. The as-prepared film with 20 wt.% BNNS displays high thermal conductivity (14.03 $W \cdot m^{-1} \cdot K^{-1}$), 103-fold higher than pure ANF film, attributing to massive continuous thermal conduction pathway between BNNSs so as to facilitate fast phonon transmission. The film boasts excellent mechanical properties (stress 97.14 ± 5.17 MPa, strain 19.36 ± 0.35%), high degradation temperature (~ 542 °C), a moderate dielectric constant (~ 6.9 at 10^4 Hz), together with low dielectric loss (~ 0.026 at 10^4 Hz). Meanwhile, the film reveals high breakdown voltage (310 $MV \cdot m^{-1}$) and volume resistivity (10^{13} Ω·cm). Notably, these dielectric properties remain largely unchanged over a wide temperature range (25 to 200 °C).

KEYWORDS

multifunctional composites, thermal properties, mechanical properties, dielectric properties

1 Introduction

Dielectric polymers, with excellent integration of light quality, easy processability, low cost, and superior corrosion resistance, have been extensively utilized as insulating materials of high-temperature electric power devices, flexible electronics, and energy storage [1–5]. However, for most dielectric polymers, thermal conductivity is so low (≈ 0.1–0.5 $W \cdot m^{-1} \cdot K^{-1}$ at room temperature) that heat aggregation originating from the operation of high-energy electronic devices cannot be quickly removed and brings about internal temperature rise of electronic equipment, which ultimately has a negative impact on the performance of the instrument [6–10]. To make matters worse, when the electronic equipment runs for a long time under high-temperature condition, conventional dielectric materials with flexible and soft segments possess an inferior glass transition temperature and low temperature stability [11, 12], which results in the failure of material mechanics and dielectric properties, and gives rise to immeasurable losses. For instance, biaxially oriented polypropylene dielectric polymer exhibits low dielectric constant ($\varepsilon \approx 2.25$) and low loss factor at room temperature. Unfortunately, the above-mentioned dielectric polymer is only capable of stable operation below 85 °C owing to the low melting temperature [13, 14]. Therefore, research on the development of nanocomposite films simultaneously with high thermal conductivity, stable mechanical properties, and low dielectric performances over a broad range of temperatures remains a challenge.

For the sake of addressing this problem, a universal strategy is provided to improve thermal conductivity of dielectric polymers via introducing high thermal conductive nanofillers into polymers [15–20]. As a typical representative, hexagonal boron nitride is endowed with high thermal conductivity (~ 400 $W \cdot m^{-1} \cdot K^{-1}$), high thermal decomposition temperature (> 800 °C) in air conditions, wide band gap (5.9 eV), low dielectric constant (~ 3.9), along with high breakdown strength (~ 800 $kV \cdot mm^{-1}$), allowing it to be a promising nanofiller in high thermal conductive dielectric polymers [21–28]. As the matrix of composite materials, integrated aramid nanofiber (ANF) has attracted increasing attention and research by virtue of its high strength (~ 3.6 GPa) and modulus (~ 90 GPa), thermal stability property, and low dielectric constant, since it was first exfoliated into stable dispersion through the deprotonation of aramid fiber by Kotov et al. in 2011 [29–32]. Based on the above-mentioned advantages of boron nitride nanosheet (BNNS) and ANF, the BNNS/ANF nanocomposite materials have been prepared using various technologies [33, 34]. For example, Ajayan et al. prepared BNNS/ANF dielectric nanocomposite film through a vacuum-assisted layer-by-layer filtration technique, showing certain thermal conductivity (2.40 ± 0.20 $W \cdot m^{-1} \cdot K^{-1}$) and a stable dielectric constant over a broad temperature range [35]. However, the thermal performance of film is relatively low, production process is time-consuming, and mass production cannot be easy to implement, which significantly hinders the prospect of its industrial application [36]. Hence, it is urgently needed to exploit a new way to prepare high thermal conductive nanocomposites on a large scale with a simultaneous combination of mechanical and

Address correspondence to tengchao2011@126.com

dielectric properties in a wide temperature range.

In this work, ANF dispersion was obtained by solvent exfoliation method. BNNS paste was prepared through ball milling exfoliation technology. The large-scale BNNS/ANF film was obtained by blade-coating approach and sol-gel transformation procedure (Scheme 1) [37, 38]. The film exhibits ordered layered structure and is conferred excellent thermal conductivity in-plane direction (14.03 $W \cdot m^{-1} \cdot K^{-1}$, 103-fold higher than that of pure ANF film) [7], and high mechanical properties (stress 97.14 ± 5.17 MPa, strain 19.36 ± 0.35%) at 20 wt.% BNNS loading. Additionally, the BNNS/ANF film possesses good dielectric properties (moderate dielectric constant, low dielectric loss, and high breakdown voltage). Fortunately, these dielectric properties remain largely unchanged in the temperature range from 25 to 200 °C, which guarantees this large-scale, layered nanocomposite film's potential applications in broad temperature-condition electric equipment fields.

2 Experimental section

2.1 Materials

Hexagonal boron nitride (h-BN, 99.50%) powder was obtained from Goodfellow Cambridge Ltd. Aramid short-cut fiber was bought from DuPont (Kevlar 29). Dimethyl sulfoxide (DMSO) and potassium hydroxide (KOH) were purchased by Sinopharm Chemical Reagent Co., Ltd.

2.2 Preparation of ANF dispersion and BNNS paste

4 g of aramid fiber and 6 g of KOH were mixed with 196 g of DMSO solvent. The above-mentioned mixture was evenly dispersed by mechanical stirring for 3 days at room temperature, forming a viscous dark red ANF dispersion (2 wt.%). BNNS paste was prepared from h-BN powder through a liquid phase exfoliation technology. In brief, 45 g of h-BN powder, 1.4 kg of ZrO_2 balls with a diameter of 0.5 mm, and 300 g of DMSO solvent were added into a stainless tank, and were grinded for 72 h. After ball-milling process, the BNNS paste was obtained.

2.3 Preparation of BNNS/ANF film

The BNNS/ANF film was fabricated through a unique sol–gel transformation approach. The ANF dispersion was compounded with BNNS paste and stirred for 8 h, forming a viscous sol. The sol was poured into a glass mould and immersed into deionized water to exchange solvent for 12 h, forming a white hydrogel. Afterwards, the hydrogel was dried in a vacuum drying oven at 45 °C for 12 h, obtaining the BNNS/ANF film. BNNS/ANF films with different ratios of BNNS to ANF (0/100, 20/80, 40/60, 60/40, and 80/20) were prepared by a sol–gel transformation process, controlled by altering the added amount of BNNS and ANF in sol.

2.4 Characterization

Microstructures of BNNS and ANF were observed by a transmission electron microscopy (TEM) (JEM-2100, JEOL). Morphologies of ANF, BNNS, and BNNS/ANF films were tested by a scanning electron microscopy (SEM) (Regulus 8100, Hitachi). The size and thickness of BNNS were performed using an atomic force microscopy (AFM, Dimension Icon, Bruker). Tensile property was examined by an electronic universal testing machine (KXWW-05C, Chengde Kebiao Testing Instrument Manufacturing Co., Ltd.), the width of sample strip was 5 mm, the gauge length of sample strip was 10 mm, and a load speed was 1 $mm \cdot min^{-1}$. Thermal stability of pristine ANF film, pristine BNNS film, and BNNS/ANF films were measured using a thermogravimetric analyzer (TGA 5500, Netzsch) under air atmosphere with a heating rise rate of 10 $°C \cdot min^{-1}$. In-plane and through-plane thermal diffusion coefficients were obtained by the laser flash method (LFA 467 NanoFlash, Netzsch) at room temperature. Thermal conductivity was calculated from the equation $\lambda = \alpha \times C_p \times \rho$, where λ stands for thermal conductivity, α is thermal diffusivity coefficient, C_p represents heat capacity, and ρ is density. Density was obtained according to the calculation of weight and sample dimension. Temperature distribution images of the pristine ANF film and nanocomposite films were recorded by an infrared thermograph (226s, Fotric Inc.). Dielectric properties were measured by a precision LCR meter (Keysight, E4980A, USA) at various temperatures in the environmental chamber. Dielectric strength was measured in silicone oil by using a breakdown voltage tester (ET2671B, Nanjing Entai Withstand Voltage Tester). Volume resistivity was obtained with an insulation resistance tester (6517B, Keithley).

3 Results and discussion

Commercial short aramid fibers are applied for raw materials to obtain ANF (Fig. 1(a)). Wherein, the yellow aramid fibers exhibit a uniform and cylindrical microstructure (Figs. 1(b) and 1(c)) with fiber diameter ranging from 11.0 to 16.5 μm at the microscopic

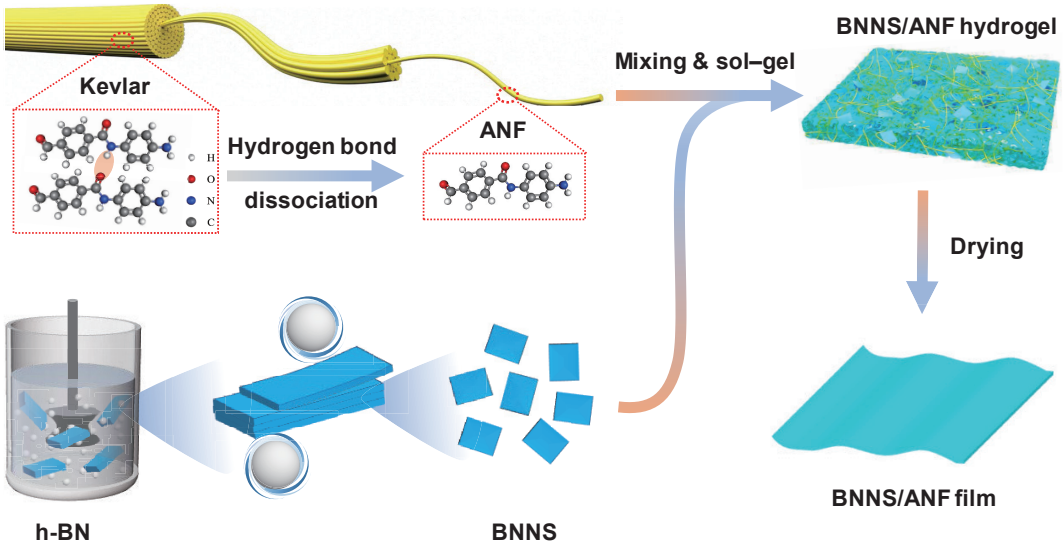

Scheme 1 Schematic diagram of preparation of the BNNS/ANF film.

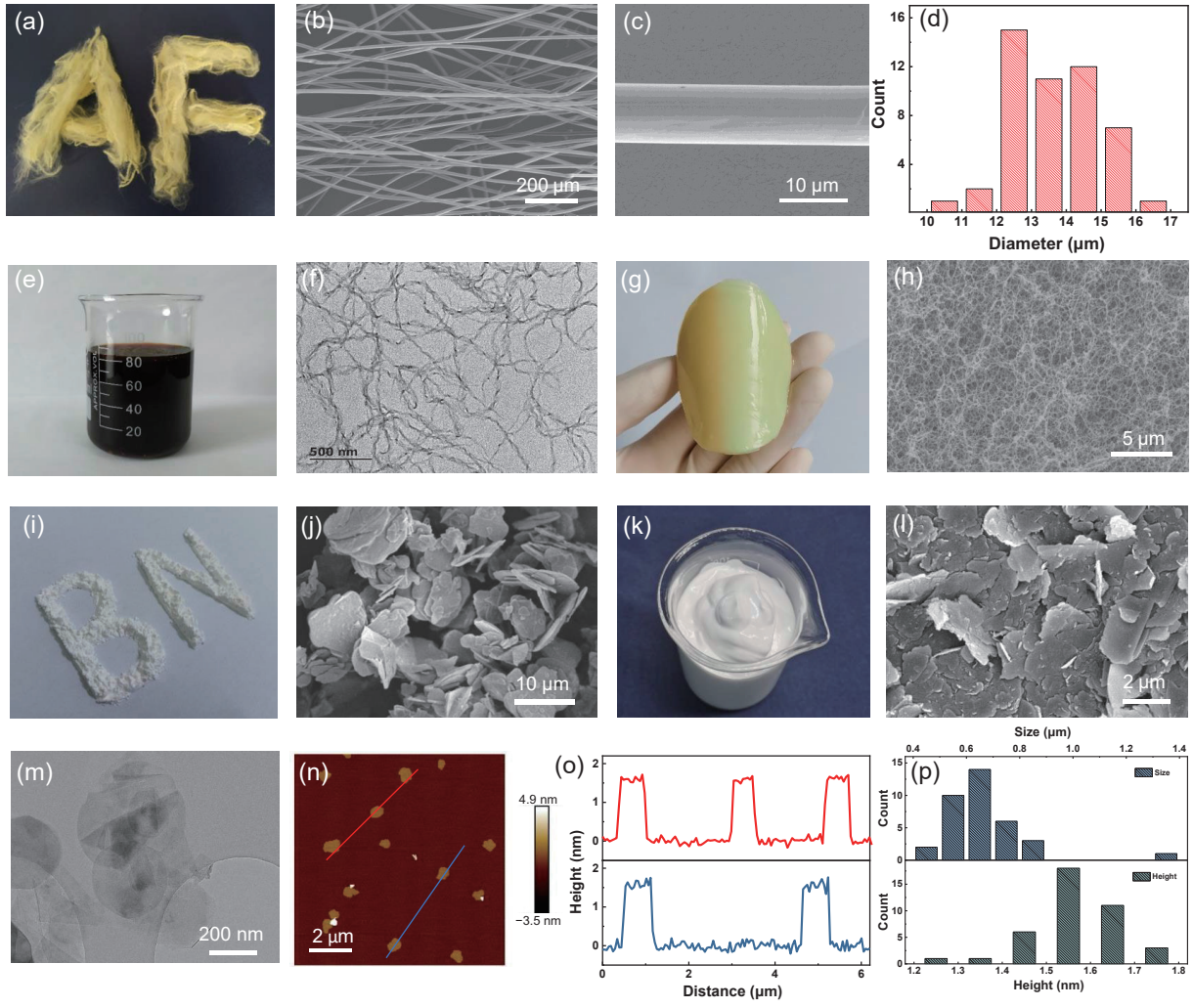

Figure 1 (a) Photograph of aramid fibers. (b) and (c) SEM images of aramid fibers. (d) The diameter distribution diagram of aramid fibers. (e) The concentration of ANF dispersion is 2 wt.%. (f) TEM image of exfoliated ANFs. (g) Photo of ANF hydrogel. (h) SEM image of ANF aerogel. (i) Photograph of commercial BN powder. (j) SEM image of BN. (k) Optical image of BNNS paste with the concentration of 13 wt.%. (l) SEM image of the free-standing BNNS film. (m) TEM image of BNNSs. (n) and (o) AFM image and corresponding to height profile of BNNSs. (p) Statistical charts of the size and height of BNNSs.

level (Fig. 1(d)). Specifically, aramid fibers were added into DMSO solvent in the existence of KOH. After mechanical stirring for 4 days at room temperature, aramid fibers could be completely exfoliated into ANFs, yielding a red ANF/DMSO dispersion with mass percent of 2 wt.% ANF (Fig. 1(e)). After dilution, the obtained ANF displays Tyndall effect indicating well dispersed in DMSO (Fig. S1(a) in the Electronic Supplementary Material (ESM)). The explanation for exfoliated mechanism seems to be that hydrogen atoms of amide groups in the polymer chains are gradually deprotonated in the context of strong alkalis, and then the hydrogen bonding interactions between polymer chains are sharply weakened, thereby forming negatively charged ANFs [39, 40]. This electrostatic rejection between ANFs not only makes the ANF/DMSO dispersion remain stable but also incorporates easily into nanocomposites [41]. The exfoliated ANF reveals a branching structure as determined by TEM measurement in Fig. 1(f). Sequentially, the ANF/DMSO dispersion was converted into ANF hydrogel by a facile sol–gel process and presents a smooth surface and sufficient flexibility, demonstrating structural integrity (Fig. 1(g)). After freeze-drying procedure, the aerogel was fabricated and maintained the inherent porous network structure of hydrogel, which is composed of generous nanofibers (Fig. 1(h)). There is devastating proof that aramid fibers are effectively split into ANFs.

Boron nitride (BN) power appears in white (Fig. 1(i)), the size and thickness of BN powder are on the micron scale, revealing lamellar structure as observed from SEM images (Fig. 1(j) and Fig. S2 in the ESM). The BN powder was incorporated into DMSO solvent, and exfoliated for 72 h by ball-milling technology. The BNNS/DMSO paste with the concentration as high as 13 wt.% was obtained, revealing a mountain peak-like shape and low liquidity (Fig. 1(k)). After dilution, the as-prepared BNNS can be well dispersed in DMSO with an obvious Tyndall effect (Fig. S1(b) in the ESM). At the microscopic level, bulk BN was exfoliated successfully into ultrathin nanosheets as determined by SEM and TEM images (Figs. 1(l) and 1(m)). Compared with BN powder, the resultant BNNSs have lateral size ranging from 0.48 to 1.33 μm and thickness from 1.28 to 1.75 nm, corresponding to 3–6 layers (Figs. 1(n)–1(p) and Fig. S3 in the ESM) [26]. In brief, the above-mentioned characterizations and analyses confirm the successful preparation of BNNSs through the high-energy ball-milling process.

The BNNS/ANF nanocomposite films were prepared by the sol–gel transformation process displayed in Scheme 1. More specifically, the aforementioned BNNS paste was firstly compounded with ANF/DMSO dispersion and magnetically stirred for 8 h at room temperature, forming a uniform and buff BNNS/ANF sol and then poured into a mould (Fig. 2(a_1)). Wherein, the weight ratio of BNNS to ANF was equal to 20:80. After blade-coating procedure, the BNNS/ANF sol with uniform thickness (2 mm) was formed (Fig. 2(a_2)), and right after exposed to deionized water for gradually converting into hydrogel

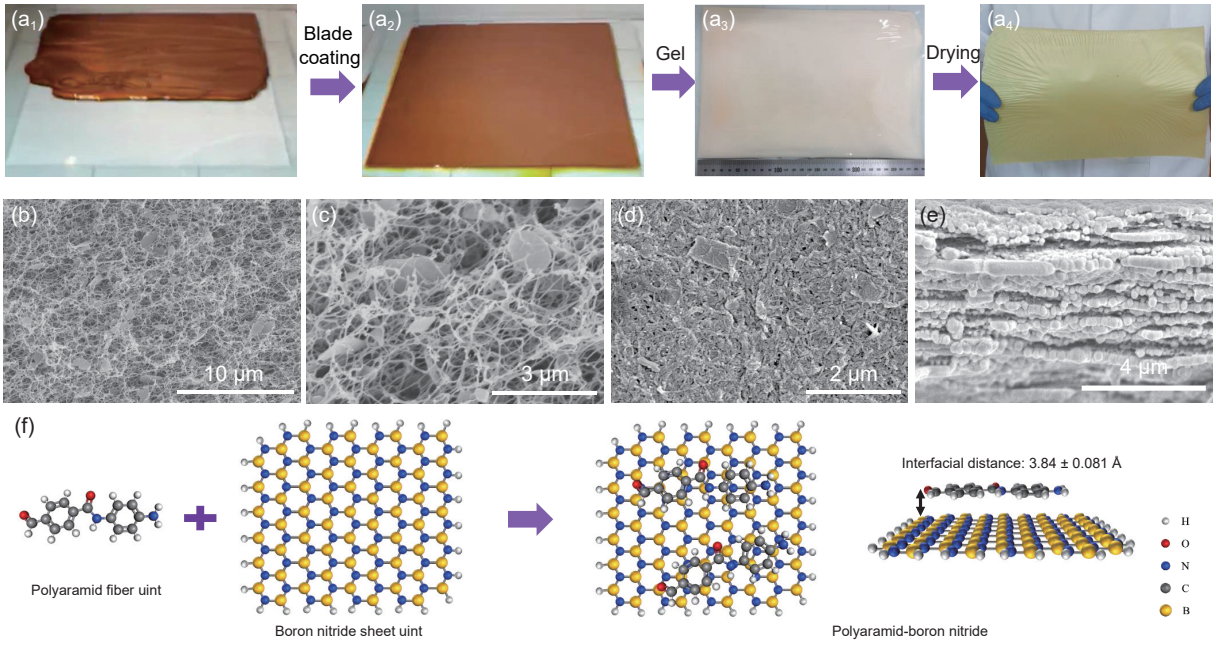

Figure 2 (a_1)–(a_4) Preparation process diagram of large-scale 20 wt.% BNNS/ANF nanocomposite film. (b) and (c) SEM images of the BNNS/ANF hydrogel after freeze-drying treatment, displaying a large number of BNNS platelets distributed into the interconnected ANF network. (d) and (e) SEM images of BNNS/ANF surface and cross-section. (f) Molecular structure models and interfacial distance of polyaramid fiber and boron nitride.

(Fig. 2(a_3)). In conversion process, the as-resulting BNNS/ANF hydrogel is interconnected by hydrogen bonding, that is, the addition of water makes the negatively charged ANFs assemble into gel networks through partial re-protonation process to re-build the hydrogen bonding between aramid nanofibers [42]. As illustrated from SEM images, ANFs inside the hydrogel boast an interconnected porous network and abundant BNNSs are well embedded into the network (Fig. 2(b)). The enlarged SEM image further determines that ANF tightly adheres to the surface of BNNS (Fig. 2(c) and Fig. S4(a) in the ESM). This phenomenon has been studied from the view of molecular structure as shown in Fig. 2(f), attributing to the fact that the ground state interfacial distance between the polyaramid fiber unit and boron nitride sheet unit is about 3.84 ± 0.081 Å, resulting in π–π interaction force between ANF's polymer backbone and BNNS's basal plane (Fig. 2(d)) [35]. After vacuum-drying process, the as-synthesized BNNS/ANF film with a width of 70 mm and a length of 154 mm reveals the potential for large-scale preparation (Fig. 2(a_4)). Compared with BNNS/ANF gel film, the thickness of BNNS/ANF film has a significantly reduction from 2.0 mm to 42 μm, ascribing to capillary forces during the evaporation of water. The BNNS/ANF film displays ordered layered structure shown in Fig. 2(e) and Fig. S4(b) in the ESM. Fourier transform infrared spectra were used to analyze structure of the nanocomposites (Fig. S5 in the ESM).

The BNNS/ANF nanocomposite film possesses an outstanding mechanical behavior. On the one hand, the film can be folded into arbitrary shapes, such as boat, crane, and aircraft, and is extremely flexible and foldable as shown in Figs. 3(a_1)–3(a_3). As presented in Figs. 3(b_1)–3(b_3), the film was bent at 180° with a bending radius of 506 and 101 μm, no cracks existed in the film surface, further indicating excellent flexibility. On the other hand, the mechanical performances including tensile strength, strain, toughness, and modulus of the BNNS/ANF nanocomposite film were measured in the tensile mode, and the corresponding strain–stress curves for the films with different BNNSs loadings were illustrated in Figs. 3(c)–3(e) and Fig. S6 in the ESM. As anticipated, at BNNSs mass percent of 0 wt.%, 20 wt.%, 40 wt.%, 60 wt.%, and 80 wt.%, tensile strain and strength of the BNNS/ANF nanocomposite film are as high as 13.19% ± 0.90% and 93.33 ± 2.45 MPa, 19.36% ± 0.35% and 97.14 ± 5.17 MPa, 8.83% ± 0.31% and 88.75 ± 1.25 MPa, 3.56% ± 0.12% and 75.62 ± 1.00 MPa, and 1.45% ± 0.10% and 38.48 ± 0.65 MPa, respectively. The toughness and modulus are in the range of 0.37 ± 0.03–14.22 ± 0.95 MJ·m^{-3} and 3.47 ± 0.21–6.03 ± 0.90 MPa, respectively. As illustrated from Figs. 3(d) and 3(e), with an increase of BNNSs mass percent, the tensile strain, strength, and toughness of the films are increased at first and then decreased. When the BNNSs loading is 20 wt.%, the strain, strength, and toughness reach the maximum values and are higher than those of the pure ANF film and BNNS film, respectively. However, as the BNNS loading further increases above 20 wt.%, the samples exhibit the reduced mechanical values, even lower than the pure ANF film. The resultant phenomenon is explained that the synergistic effects of the slipping between BNNSs, continuous 3D ANF network framework, and π–π bonding agents between BNNSs and ANFs can dissipate fracture energy to large ductility and toughness. Apart from the mechanicalproperty,theBNNS/ANFfilmexhibitsitsnonflammability (Fig. S7 in the ESM) and high thermal degradation temperature (542 °C), higher than pure ANF film (536 °C) (Fig. S8 in the ESM).

The thermal conduction property of BNNS/ANF nanocomposite film was further investigated. We measured the anisotropic thermal conductivities of BNNS/ANF films along the in-plane and through-plane direction as shown in Fig. 4(a) and Table S1 in the ESM. An appreciable increase in-plane thermal conductivity is observed with an increasing amount of BNNS from 20 wt.% to 80 wt.%, while the through-plane thermal conductivity exhibits slightly variations. When the BNNS loading reaches up to 80 wt.%, the in-plane thermal conductivity has a maximum value of 34.47 W·m^{-1}·K^{-1}, much higher than the common polymer (Table S2 in the ESM). With the accumulation of BNNS, an increasing contact between nanosheets results in the formation of a great deal of continuous thermal conduction pathways in the interior of nanocomposite film, which is conducive to phonon transmission. At the same time, the nanocomposite films with BNNS loading 20 wt.%, 40 wt.%, 60 wt.%, and 80 wt.% were simultaneously contacted with a heat source, their thermal conduction properties were assessed using infrared thermal imaging instrument. As presented in Fig. 4(b)

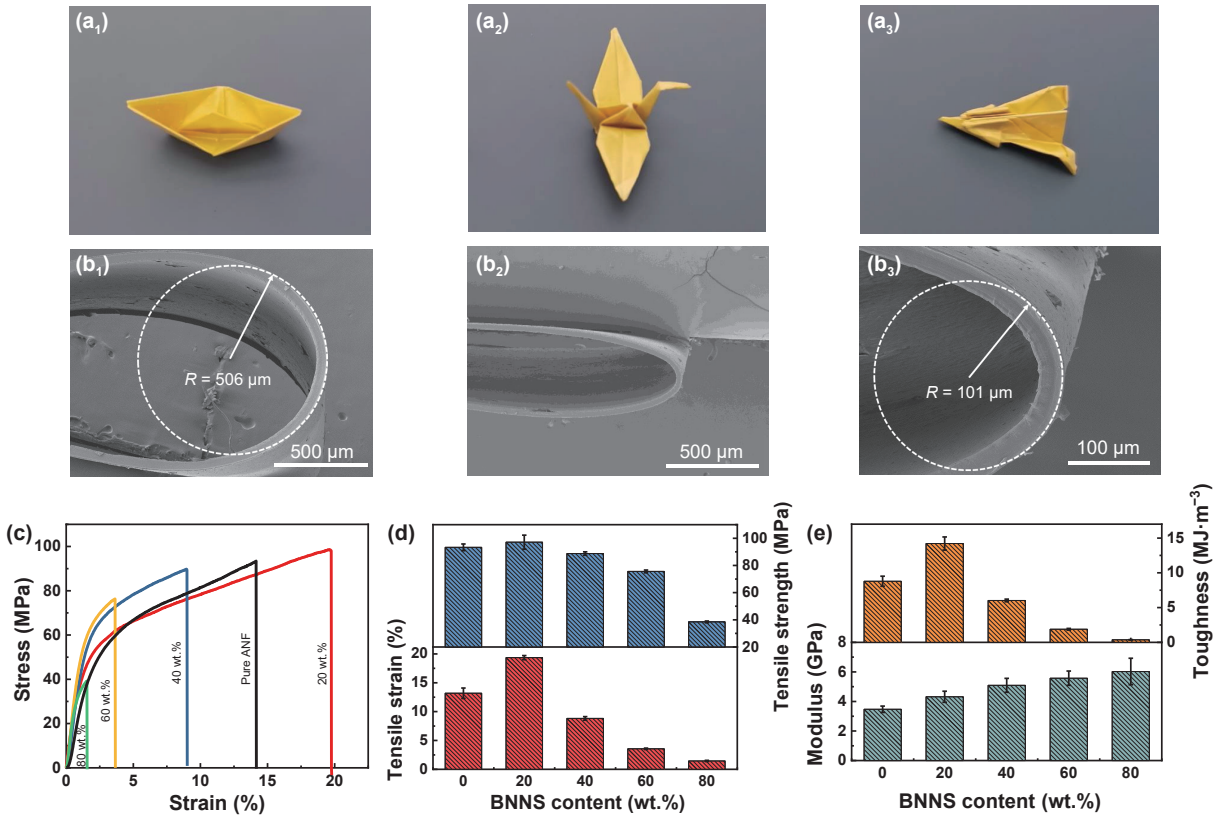

Figure 3 (a_1)–(a_3) Photograph of 20 wt.% BNNS/ANF nanocomposite film is folded into the boat, crane, and plane. (b_1)–(b_3) SEM images of BNNS/ANF film folded at 180° forming a radius of about 506 and 101 μm. (c) Tensile stress–strain curves of BNNS/ANF film with various content of BNNS. (d) and (e) Tensile stress, fracture stain, modulus, and toughness as a function of BNNS content, respectively.

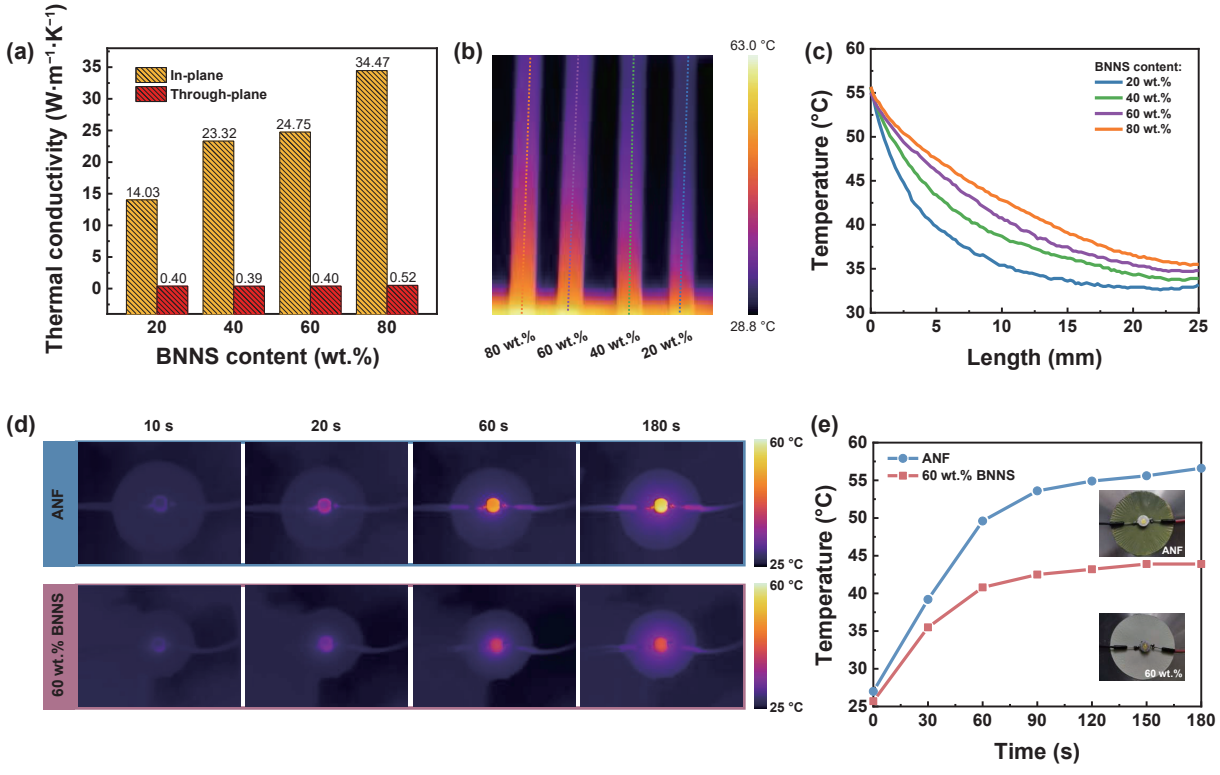

Figure 4 (a) Dependence of thermal conductivity on the weight ratio of BNNS and ANF. (b) and (c) Infrared thermal image of different BNNS content and corresponding temperature–distance curves. (d) Operating temperature versus time for thermal management of a point-like heat source. (e) Corresponding temperature changes versus time of ANF film and BNNS/ANF film.

and Fig. S9(a) in the ESM, with an increase of BNNSs loading content, the heat transfer rate of nanocomposite films has a gradual improvement. After data processing (Fig. 4(c) and Fig. S9(b) in the ESM), the temperature of films with BNNS loading content of 80 wt.% is highest than those of other contents at the same location, exhibiting superb heat transfer rate. Moreover, the BNNS/ANF film with outstanding thermal management capabilities was demonstrated to act as a flexible electronic

substrate to potentially apply in the field of electronic industry. The higher thermal responses of the BNNS/ANF film with 60 wt.% BNNS relative to a pure ANF film were achieved through monitoring surfaces temperature shift continuously in Fig. 4(d). Two 1 W light-emitting diode (LED) lamps with the same diameter 5.5 mm were firstly adhered to the surfaces of a pure ANF film and the BNNS/ANF nanocomposite film with 60 wt.% BNNSs, respectively, and connected with a 3.2 V current source. Then, the surface temperature was recorded using infrared thermal imaging instrument. It can be clearly observed that the intermediate temperature of LED lamps continues to increase as time goes on, and the heating rate is up to 9.9 °C·min^{-1} for the pure ANF film, which is almost 1.62 times than that of the BNNS/ANF film. After 180 s, the central temperature reaches balance points, which are 43.9 and 56.6 °C for BNNS/ANF and pure ANF film, respectively. In comparison with the two films, it is found that the temperature of LED lamps on nanocomposite film increases slowly during the same time period, presenting excellent thermal management performance for electronic equipment.

The dielectric constant and dielectric loss of BNNS/ANF films were measured under different BNNS contents and different temperature conditions at the frequency range from 10^2 to 10^6 Hz using an Keysight E4980A precision LCR meter. Figure 5(a) shows dielectric constant and dielectric loss of BNNS/ANF films with different BNNS loading as function of frequency at room temperature. We can see that dielectric constant of BNNS/ANF film slightly decreases with the increasing frequency from 10^2 to 10^6 Hz attributing to the polarization relaxation effect, which is consistent with Refs. [43, 44]. Meanwhile, BNNS/ANF film reveals a low dielectric loss. Moreover, dielectric constant of pure ANF film decreases from 8.0 to 5.3 with the growing loading of BNNS from 0 wt.% to 80 wt.% at a frequency of 10^4 Hz (Fig. 5(b)). This phenomenon mainly contributes to the low dielectric constant (~ 3.9) and dielectric loss (0.0002) of BNNS [45]. As shown in Fig. 5(c), the temperature changes from 25 to 200 °C, and the dielectric constant and dielectric loss remain largely unchanged. This result indicates that BNNS/ANF film exhibits thermally stable dielectric constant to eliminate "crosstalk" or charge transfer between conducting materials [35]. To further reveal the thermal effects on BNNS/ANF film, the temperature coefficient of dielectric constant (K) was obtained displayed in Fig. 5(d). We can see that the value of K decreases and then increases slightly with increasing temperature, displaying a positive value of K [44]. This result mainly attributes to the construction a thermal pathway of high conductive BNNS to deplete the heating effects. The dielectric strength was measured in insulating oil by sandwiching the BNNS/ANF film between two parallel metal electrodes (Fig. S10 in the ESM). As represented in Fig. 5(e), the dielectric strength of BNNS/ANF film is higher than that of pure ANF, because the BNNS possesses an intrinsic high dielectric strength (800 kV·mm^{-1}) and ordered layered structure. To reveal the advantages of the layered BNNS/ANF film as the dielectric polymer, a radar map was used to compare the layered BNNS/ANF film with pure ANF film (Fig. 5(f) and Table S2 in the ESM). This result indicates that the nanocomposite film exhibits an excellent integration of tensile strength, toughness, thermal conductivity, dielectric constant, and breakdown strength, obviously superior to pure ANF film.

4 Conclusions

In summary, we successfully prepared the large-scale layered BNNS/ANF film through blade-coating approach and sol–gel transformation process. The BNNS/ANF film with 20 wt.% BNNS exhibits high thermal conductivity (14.03 W·m^{-1}·K^{-1}), high mechanical properties (stress 97.14 ± 5.17 MPa, strain 19.36% ± 0.35%), high thermal stability (degradation temperature 542 °C), a moderate dielectric constant (~ 6.9), high breakdown strength (310 MV·m^{-1}), and electrically insulating (10^{13} Ω·cm). These properties attribute to the mechanical integrity and electrical insulation of interconnected ANF and the high thermal conductivity of BNNS. More importantly, the BNNS/ANF films reveal stable mechanical properties and dielectric properties (dielectric constant and dielectric loss) over a broad temperature range. This approach offers a new way for multifunctional nanocomposite films applied in high-temperature electric power devices and flexible electronics.

Acknowledgements

The authors acknowledge the financial support from the National

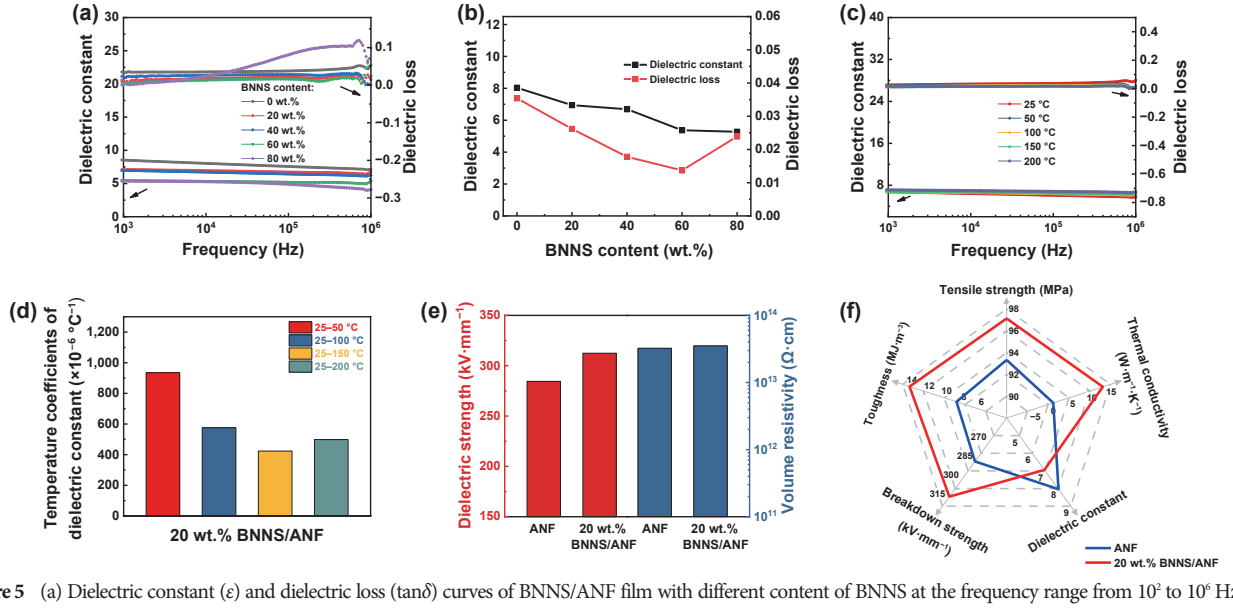

Figure 5 (a) Dielectric constant (ε) and dielectric loss (tanδ) curves of BNNS/ANF film with different content of BNNS at the frequency range from 10^2 to 10^6 Hz. (b) Dielectric constant and loss of BNNS/ANF film with different BNNS loading at a frequency of 10^4 Hz. (c) Dielectric constant and loss of BNNS/ANF films at the frequency range from 10^2 to 10^6 Hz and temperature range from 25 to 200 °C. (d) Temperature coefficient of dielectric constant of BNNS/ANF film at 1 kHz in the range of 25 to 200 °C. (e) Dielectric strength and volume resistivity and of the BNNS/ANF and pure ANF film. (f) A radar plot revealing a comparison between the BNNS/ANF film and pure ANF film.

Natural Science Foundation of China (No. 22075161).

Electronic Supplementary Material: Supplementary material (Tyndall effect of ANF and BNNS dispersion, TGA curves, SEM and AFM images, FTIR spectra, digital photographs, mechanical properties of the films, flame retardant performance, infrared thermal image, the temperature-distance curves of the films, comparison of mechanical performance, and dielectric properties and thermal conductivity of the as-prepared film with the other reported materials) is available in the online version of this article at https://doi.org/10.1007/s12274-022-4456-6.

References

[1] Hassan, Y. A.; Hu, H. L. Current status of polymer nanocomposite dielectrics for high-temperature applications. *Compos. Part A Appl. Sci. Manuf.* **2020**, *138*, 106064.

[2] Nie, R. P.; Lei, J.; Jia, L. C.; Chen, C.; Xu, L.; Li, H.; Huang, H. D.; Yu, F. M.; Li, Z. M. Significantly improved high-temperature performance of polymer dielectric via building nanosheets and confined space. *Compos. Part B Eng.* **2020**, *196*, 108108.

[3] Corma, A.; Serna, P. Chemoselective hydrogenation of nitro compounds with supported gold catalysts. *Science* **2006**, *313*, 332–334.

[4] Lokanathan, M.; Acharya, P. V.; Ouroua, A.; Strank, S. M.; Hebner R. E.; Bahadur, V. Review of nanocomposite dielectric materials with high thermal conductivity. *Proc. IEEE* **2021**, *109*, 1364–1397.

[5] Cao, L.; Wang, J. J.; Dong, J.; Zhao, X.; Li H. B.; Zhang, Q. H. Preparation of highly thermally conductive and electrically insulating PI/BNNSs nanocomposites by hot-pressing self-assembled PI/BNNSs microspheres. *Compos. Part B Eng.* **2020**, *188*, 107882.

[6] Shinde, S. L.; Ishii, S.; Dao, T. D.; Sugavaneshwar, R. P.; Takei, T.; Nanda, K. K.; Nagao, T. Enhanced solar light absorption and photoelectrochemical conversion using TiN nanoparticle-incorporated C_3N_4-C dot sheets. *ACS Appl. Mater. Interfaces* **2018**, *10*, 2460–2468.

[7] Ma, T. B.; Zhao, Y. S.; Ruan, K. P.; Liu, X. R.; Zhang, J. L.; Guo, Y. Q.; Yang, X. T.; Kong, J.; Gu, J. W. Highly thermal conductivities, excellent mechanical robustness and flexibility, and outstanding thermal stabilities of aramid nanofiber composite papers with nacre-mimetic layered structures. *ACS Appl. Mater. Interfaces* **2020**, *12*, 1677–1686.

[8] Teng, C.; Su, L. Y.; Chen, J. X.; Wang, J. F. Flexible, thermally conductive layered composite films from massively exfoliated boron nitride nanosheets. *Compos. Part A Appl. Sci. Manuf.* **2019**, *124*, 105498.

[9] Li, L.; Cao, Y. X.; Liu, X. Y.; Wang, J. F.; Yang, Y. Y.; Wang, W. J. Multifunctional MXene-based fireproof electromagnetic shielding films with exceptional anisotropic heat dissipation capability and joule heating performance. *ACS Appl. Mater. Interfaces* **2020**, *12*, 27350–27360.

[10] Han, J. K.; Du, G. L.; Gao, W. W.; Bai, H. An anisotropically high thermal conductive boron nitride/epoxy composite based on nacre-mimetic 3D network. *Adv. Funct. Mater.* **2019**, *29*, 1900412.

[11] Ryu, S. Y.; Chung, J. W.; Kwak, S. Y. Amphiphobic meta-aramid nanofiber mat with improved chemical stability and mechanical properties. *Eur. Polym. J.* **2017**, *91*, 111–120.

[12] Lei, C. X.; Zhang, Y. Z.; Liu, D. Y.; Wu, K.; Fu, Q. Metal-level robust, folding endurance, and highly temperature-stable MXene-based film with engineered aramid nanofiber for extreme-condition electromagnetic interference shielding applications. *ACS Appl. Mater. Interfaces* **2020**, *12*, 26485–26495.

[13] Azizi, A.; Gadinski, M. R.; Li, Q.; AlSaud, M. A.; Wang, J. J.; Wang, Y.; Wang, B.; Liu, F. H.; Chen, L. Q.; Alem, N. et al. High-performance polymers sandwiched with chemical vapor deposited hexagonal boron nitrides as scalable high-temperature dielectric materials. *Adv. Mater.* **2017**, *29*, 1701864.

[14] Chi, Q. G.; Gao, Z. Y.; Zhang, T. D.; Zhang, C. H.; Zhang, Y.; Chen, Q. G.; Wang, X.; Lei, Q. Q. Excellent energy storage properties with high-temperature stability in sandwich-structured polyimide-based composite films. *ACS Sustainable Chem. Eng.* **2019**, *7*, 748–757.

[15] Vu, M. C.; Mani, D.; Jeong, T. H.; Kim, J. B.; Lim, C. S.; Kang, H.; Islam, M. A.; Lee, O. C.; Park, P. J.; Kim, S. R. Nacre-inspired nanocomposite papers of graphene fluoride integrated 3D aramid nanofibers towards heat-dissipating applications. *Chem. Eng. J.* **2022**, *429*, 132182.

[16] Li, M.; Wang, M. J.; Hou, X.; Zhan, Z. L.; Wang, H.; Fu, H.; Lin, C. T.; Fu, L.; Jiang, N.; Yu, J. H. Highly thermal conductive and electrical insulating polymer composites with boron nitride. *Compos. Part B Eng.* **2020**, *184*, 107746.

[17] Zhang, L.; Deng, H.; Fu, Q. Recent progress on thermal conductive and electrical insulating polymer composites. *Compos. Commun.* **2018**, *8*, 74–82.

[18] Teng, C.; Xie, D.; Wang, J. F.; Yang, Z.; Ren, G. Y.; Zhu, Y. Ultrahigh conductive graphene paper based on ball-milling exfoliated graphene. *Adv. Funct. Mater.* **2017**, *27*, 1700240.

[19] Tang, L.; He, M. K.; Na, X.; Guan, X. F.; Zhang, R. H.; Zhang, J. L.; Gu, J. W. Functionalized glass fibers cloth/spherical BN fillers/epoxy laminated composites with excellent thermal conductivities and electrical insulation properties. *Compos. Commun.* **2019**, *16*, 5–10.

[20] Gu, J. W.; Meng, X. D.; Tang, Y. S.; Li, Y.; Zhuang, Q.; Kong, J. Hexagonal boron nitride/polymethyl-vinyl siloxane rubber dielectric thermally conductive composites with ideal thermal stabilities. *Compos. Part A Appl. Sci. Manuf.* **2017**, *92*, 27–32.

[21] Liu, J. C.; Li, W. W.; Guo, Y. F.; Zhang, H.; Zhang, Z. Improved thermal conductivity of thermoplastic polyurethane via aligned boron nitride platelets assisted by 3D printing. *Compos. Part A Appl. Sci. Manuf.* **2019**, *120*, 140–146.

[22] Chen, Y.; Kang, Q.; Jiang, P. K.; Huang, X. Y. Rapid, high-efficient and scalable exfoliation of high-quality boron nitride nanosheets and their application in lithium-sulfur batteries. *Nano Res.* **2020**, *14*, 2424–2431.

[23] Li, L. H.; Chen, Y. Atomically thin boron nitride: Unique properties and applications. *Adv. Funct. Mater.* **2016**, *26*, 2594–2608.

[24] Li, Y.; Tian, X J.; Yang, W.; Li, Q.; Hou, L. Q.; Zhu, Z. X.; Tang, Y. S.; Wang, M. J.; Zhang, B.; Pan, T. et al. Dielectric composite reinforced by *in-situ* growth of carbon nanotubes on boron nitride nanosheets with high thermal conductivity and mechanical strength. *Chem. Eng. J.* **2019**, *358*, 718–724.

[25] Wang, T. T.; Wei, C. M.; Yan, L.; Liao, Y.; Wang, G. L.; Zhao, L. H.; Fu, M. L.; Ren, J. W. Thermally conductive, mechanically strong dielectric film made from aramid nanofiber and edge-hydroxylated boron nitride nanosheet for thermal management applications. *Compos. Interfaces* **2021**, *28*, 1067–1080.

[26] Pakdel, A.; Bando, Y.; Golberg, D. Nano boron nitride flatland. *Chem. Soc. Rev.* **2014**, *43*, 934–959.

[27] Wu, K.; Fang, J. C.; Ma, J. R.; Huang, R.; Chai, S. G.; Chen, F.; Fu, Q. Achieving a collapsible, strong, and highly thermally conductive film based on oriented functionalized boron nitride nanosheets and cellulose nanofiber. *ACS Appl. Mater. Interfaces* **2017**, *9*, 30035–30045.

[28] Han, Y. X.; Shi, X. T.; Yang, X. T.; Guo, Y. Q.; Zhang, J. L.; Kong, J.; Gu, J. W. Enhanced thermal conductivities of epoxy nanocomposites via incorporating *in-situ* fabricated hetero-structured SiC-BNNS fillers. *Compos. Sci. Technol.* **2020**, *187*, 107944.

[29] Yang, B.; Wang, L.; Zhang, M. Y.; Luo, J. J.; Lu, Z. Q.; Ding, X. Y. Fabrication, applications, and prospects of aramid nanofiber. *Adv. Funct. Mater.* **2020**, *30*, 2000186.

[30] Yang, M.; Cao, K. Q.; Sui, L.; Qi, Y.; Zhu, J.; Waas, A.; Arruda, E. M.; Kieffer, J.; Thouless, M. D.; Kotov, N. A. Dispersions of aramid nanofibers: A new nanoscale building block. *ACS Nano* **2011**, *5*, 6945–6954.

[31] Zhang, B.; Wang, W. C.; Tian, M.; Ning, N. Y.; Zhang, L. Q. Preparation of aramid nanofiber and its application in polymer reinforcement: A review. *Eur. Polym. J.* **2020**, *139*, 109996.

[32] Roy, S.; Zhang, X.; Puthirath, A. B.; Meiyazhagan, A.; Bhattacharyya, S.; Rahman, M. M.; Babu, G.; Susarla, S.; Saju, S. K.; Tran, M. K. et al. Structure, properties and applications of

two-dimensional hexagonal boron nitride. *Adv. Mater.* **2021**, *33*, 2101589.

[33] Zhao, Y.; Li, X.; Shen, J. N.; Gao, C. J.; Van Der Bruggen, B. The potential of Kevlar aramid nanofiber composite membranes. *J. Mater. Chem. A* **2020**, *8*, 7548–7568.

[34] Wu, K.; Wang, J. M.; Liu, D. Y.; Lei, C. X.; Liu, D.; Lei, W. W.; Fu, Q. Highly thermoconductive, thermostable, and super-flexible film by engineering 1D rigid rod-like aramid nanofiber/2D boron nitride nanosheets. *Adv. Mater.* **2020**, *32*, 1906939.

[35] Rahman, M. M.; Puthirath, A. B.; Adumbumkulath, A.; Tsafack, T.; Robatjazi, H.; Barnes, M.; Wang, Z. X.; Kommandur, S.; Susarla, S.; Sajadi, S. M. et al. Fiber reinforced layered dielectric nanocomposite. *Adv. Funct. Mater.* **2019**, *29*, 1900056.

[36] Zhang, J. Z.; Kong, N.; Uzun, S.; Levitt, A.; Seyedin, S.; Lynch, P. A.; Qin, S.; Han, M. K.; Yang, W. R.; Liu, J. Q. et al. Scalable manufacturing of free-standing, strong $Ti_3C_2T_x$ mxene films with outstanding conductivity. *Adv. Mater.* **2020**, *32*, 2001093.

[37] Zeng, F. Z.; Chen, X. H.; Xiao, G.; Li, H.; Xia, S.; Wang, J. F. A bioinspired ultratough multifunctional mica-based nanopaper with 3D aramid nanofiber framework as an electrical insulating material. *ACS Nano* **2020**, *14*, 611–619.

[38] Wang, Y. J.; Xia, S.; Li, H.; Wang, J. F. Unprecedentedly tough, folding-endurance, and multifunctional graphene-based artificial nacre with predesigned 3D nanofiber network as matrix. *Adv. Funct. Mater.* **2019**, *29*, 1903876.

[39] Han, Y. X.; Ruan, K. P.; Gu, J. W. Janus (BNNS/ANF)-(AgNWs/ANF) Thermal conductivity composite films with superior electromagnetic interference shielding and joule heating performances. *Nano Res.* **2022**, *15*, 4747–4755.

[40] Weng, C. X.; Xing, T. L.; Jin, H.; Wang, G. R.; Dai, Z. H.; Pei, Y. M.; Liu, L. Q.; Zhang, Z. Mechanically robust ANF/MXene composite films with tunable electromagnetic interference shielding performance. *Compos. Part A Appl. Sci. Manuf.* **2020**, *135*, 105927.

[41] Kwon, S. R.; Harris, J.; Zhou, T. Y.; Loufakis, D.; Boyd, J. G.; Lutkenhaus, J. L. Mechanically strong graphene/aramid nanofiber composite electrodes for structural energy and power. *ACS Nano* **2017**, *11*, 6682–6690.

[42] Lin, M. Y.; Li, Y. H.; Xu, K.; Ou, Y. H.; Su, L. F.; Feng, X.; Li, J.; Qi, H. S.; Liu, D. T. Thermally conductive nanostructured, aramid dielectric composite films with boron nitride nanosheets. *Compos. Sci. Technol.* **2019**, *175*, 85–91.

[43] Yang, L.; Qiu, J. H.; Ji, H. L.; Zhu, K. J.; Wang, J. Enhanced dielectric and ferroelectric properties induced by TiO_2@MWCNTs nanoparticles in flexible poly(vinylidene fluoride) composites. *Compos. Part A Appl. Sci. Manuf.* **2014**, *65*, 125–134.

[44] Liu, S. N.; Tu, L.; Liu, C. C.; Tong, L. F.; Bai, Z. X.; Lin, G.; Jia, K.; Liu, X. B. Interfacial crosslinking enabled super-engineering polymer-based composites with ultra-stable dielectric properties beyond 350 °C. *J. Alloys Compd.* **2022**, *891*, 161952.

[45] Li, M. J.; Zhu, Y. F.; Teng, C. Q. Facial fabrication of aramid composite insulating paper with high strength and good thermal conductivity. *Compos. Commun.* **2020**, *21*, 100370.